Toward Reversible and Moisture-Tolerant Aprotic Lithium-Air Batteries

Joule

CellPress

Article

Toward Reversible and Moisture-Tolerant Aprotic Lithium-Air Batteries

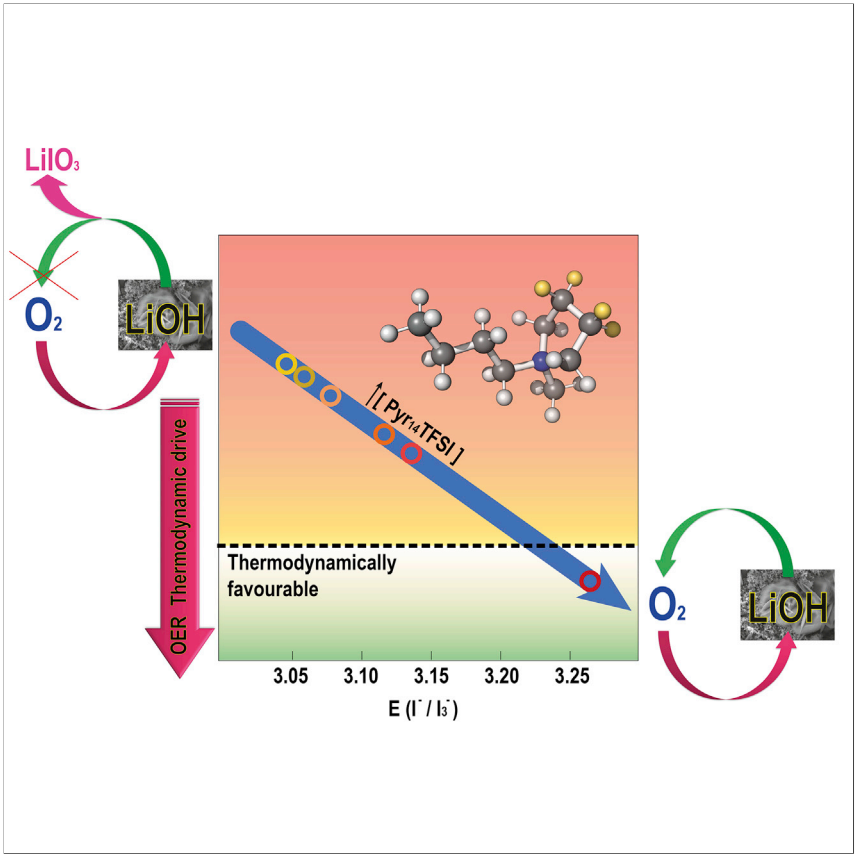

Li-air batteries have attracted significant attention due to their very high energy density, comparable to that of fossil fuels. For their development, a stable discharge product that can be reversibly decomposed during charge needs to be developed. LiOH is a promising candidate, but questions concerning the reversibility of the charge process have been raised. Here, we report for the first time Li-O_2 cells that can reversibly cycle via LiOH by using water and an ionic liquid as additives in the electrolyte.

Israel Temprano, Tao Liu, Enrico Petrucco, James H.J. Ellison, Gunwoo Kim, Erlendur Jónsson, Clare P. Grey

cpg27@cam.ac.uk

HIGHLIGHTS

Iodide-mediated Li-O_2 cells can reversibly cycle via LiOH with low overpotential

Electrolyte additives can increase the redox potential of the I^-/I_3^- couple

At sufficiently high I^-/I_3^- redox potentials, OER from LiOH becomes favorable

Temprano et al., Joule 4, 2501–2520
November 18, 2020
https://doi.org/10.1016/j.joule.2020.09.021

Joule

CellPress

Article

Toward Reversible and Moisture-Tolerant Aprotic Lithium-Air Batteries

Israel Temprano,[1] Tao Liu,[1,4] Enrico Petrucco,[2] James H.J. Ellison,[1] Gunwoo Kim,[1] Erlendur Jónsson,[1,3] and Clare P. Grey[1,5,*]

SUMMARY

The development of moisture-tolerant, LiOH-based non-aqueous Li-O_2 batteries is a promising route to bypass the inherent limitations caused by the instability of their typical discharge products, LiO_2 and Li_2O_2. The use of the I^-/I_3^- redox couple to mediate the LiOH-based oxygen reduction and oxidation reactions has proven challenging due to the multiple reaction paths induced by the oxidation of I^- on cell charging. In this work, we introduce an ionic liquid to a glyme-based electrolyte containing LiI and water and demonstrate a reversible LiOH-based Li-O_2 battery cycling that operates via a 4 e^-/O_2 process with a low charging overpotential (below 3.5 V versus Li/Li^+). The addition of the ionic liquid increases the oxidizing power of I_3^-, shifting the charging mechanism from IO^-/IO_3^- formation to O_2 evolution.

INTRODUCTION

In light of recent commitments from several European countries to ban the sale of internal combustion engine vehicles in the coming decades,[1,2] the race to develop electrical storage strategies beyond the capabilities of lithium-ion batteries is intensifying considerably. Among the many different options, Li-air batteries have attracted significant attention due to their comparable energy density to fossil fuels.[3]

Non-aqueous Li-air batteries (LABs) are generally composed of a lithium-metal anode, an organic-based lithium-ion conducting liquid electrolyte, and a porous, typically carbon-based, cathode. During discharge, O_2 is reduced at the cathode (the oxygen reduction reaction, ORR), which then combines with lithium ions in solution, forming insoluble discharge products that fill up the porous structure of the carbon electrode. The discharge product is oxidized during charge, with O_2 being released back to the atmosphere (the oxygen evolution reaction, OER).[4]

Despite its potential, several fundamental challenges remain to be overcome to allow the successful development of a practical non-aqueous LAB.[4–8] Among these challenges, the instability of the typical discharge products (LiO_2 and Li_2O_2) in the presence of moisture and CO_2 represents a fundamental stumbling block.[9,10] Recently, it has been shown that lithium hydroxide (LiOH) can be formed as a discharge product in moisture-tolerant LABs with a high capacity and low charge overpotential using either LiI as a redox mediator or Ru as a catalyst in a wet organic electrolyte.[11–13] However, it is widely believed that LiOH is not reversible due to (1) the half-cell potential of the LiOH OER under standard state (aqueous) conditions being higher than that of the Li_2O_2 OER, given the higher thermodynamic stability of the former; (2) the detection on charge of oxidation products such as

Context & Scale

Li-air batteries have attracted significant attention as a strategy to develop affordable and sustainable electrical storage with higher energy density than current lithium-ion batteries, having theoretical energy densities that rival those of fossil fuels and, in their simplest form, avoiding the use of resource-limited transition metal oxides. The formation of LiOH as discharge product is a promising route to bypass some of the most acute challenges this very young technology faces. However, one critical challenge is to charge the battery reversibly, evolving oxygen gas at low overpotentials. While previous studies have indicated that the I^-/I_3^- redox couple may not have sufficient thermodynamic drive for the oxygen evolution reaction, here we demonstrate that additives in the electrolyte (ionic liquid and water) can increase the I^-/I_3^- equilibrium redox potential sufficiently to enable a reversible charge process at low overpotentials.

IO_3^-,[12,14,15] and $DMSO_2$,[13] which originate from the redox mediator and the solvents, respectively; and (3) little or no oxygen evolution being observed in gas analysis experiments.[14] These observations have given rise to doubts as to whether the iodide/triiodide (I^-/I_3^-) redox system is capable of sustaining reversible ORR/OER chemistry via LiOH formation and decomposition.[14–17]

The electrochemical behavior of the iodide/triiodide redox system has been extensively reported in the literature, and it is by now well established that the (I^-/I_3^-) redox potential is solvent dependent[12,18–20]: the oxidizing power of I_3^- can be readily tailored by means of adjusting the physicochemical parameters of the electrolyte (dielectric constant, ionic strength, Gutmann acceptor/donor numbers, etc.). Ionic liquids (ILs) have been shown to alter the solvation/coordination environments of this redox system, again substantially affecting the (I^-/I_3^-) redox potential,[18] while still allowing high ionic conductivity and reducing solvent volatility.[21–28] However, the high viscosity of ILs, which reduces the O_2 diffusion coefficients, and the low O_2 solubility are disadvantageous for LAB performance.[29] The presence of water has been shown to enhance the solution-transfer of discharge products and redox mediators,[12,30–33] reducing the charge overpotential and therefore the level of parasitic reactions, as well as fundamentally affecting the activity of the (I^-/I_3^-) redox system during discharge.[11,14,34] Thus, the combination of LiI as redox mediator with water and an ionic liquid is a potentially good strategy for efficiently tailoring the electrolyte properties in Li-O_2 batteries.

In this work, we report a step forward toward the realization of a viable moisture-tolerant LAB, by reversibly cycling LiOH with low charging overpotentials in cells with LiI as a redox mediator and H_2O and 1-butyl-1-methyl-pyrrolidinum-bis(trifluoromethanesulfonyl)imide ($Pyr_{14}TFSI$) as additives in a low-volatility electrolyte. $Pyr_{14}TFSI$ is one of the most widely studied ILs in relation to Li-O_2 batteries, showing high stability toward superoxide species and a relatively high Li^+ diffusion coefficient.[24,28,29,31,35–37] We find that the inclusion of $Pyr_{14}TFSI$ is crucial for the reversibility of the electrochemical formation/decomposition of LiOH as demonstrated by the observation of a 4 e^-/O_2 OER using *operando* online electrochemical mass spectrometry (OEMS). OER from LiOH decomposition is further confirmed by OEMS experiments with (electrochemically) preloaded electrodes, as well as isotopic labeling. The suppression of the side reactions to form oxygenated iodine species (IO^-, IO_3^-), which trap the oxygen during charge, is also observed, and the mechanistic considerations of the oxygen evolution versus iodate formation are discussed in the context of the thermodynamic driving forces for both reactions. The effects of the IL and water with respect to the activity of iodine are also investigated through molecular dynamic (MD) simulations.

RESULTS AND DISCUSSION

A 4 e^-/O_2 Oxygen Evolution Reaction

Li-O_2 cells were constructed with a lithium-metal anode, an anolyte consisting of 300 mM LiTFSI in tetraethylene glycol dimethyl ether (G4), a lithium-ion conducting glass ceramic (LICGC-Ohara AG010) separating the two electrolytes, a catholyte containing 700 mM LiTFSI, 50 mM LiI, 900 mM $Pyr_{14}TFSI$, and 5,000 ppm H_2O in G4, and a mesoporous carbon black cathode (Ensaco-P150). The LICGC serves to prevent redox shuttling (I^-/I_3^-) and reaction of catholyte additives with the Li anode, since redox mediator shuttling is a possible source of "artificial" capacity, the oxidized species such as I_3^- being reduced at the anode and then migrating back to the cathode to be reoxidized.[14] These cells were evaluated with *operando* OEMS by capacity-limiting galvanostatic cycling, in order to keep the levels of water within limits

[1]Department of Chemistry, University of Cambridge, Cambridge CB2 1EW, UK

[2]Johnson Matthey Technology Centre, Blounts Court, Sonning Common, Reading RG4 9NH, UK

[3]Department of Physics, Chalmers University of Technology, Gothenburg 41296, Sweden

[4]Present address: Shanghai Key Laboratory of Chemical Assessment and Sustainability, Department of Chemistry, Tongji University, Shanghai 200092, China

[5]Lead Contact

*Correspondence: cpg27@cam.ac.uk

https://doi.org/10.1016/j.joule.2020.09.021

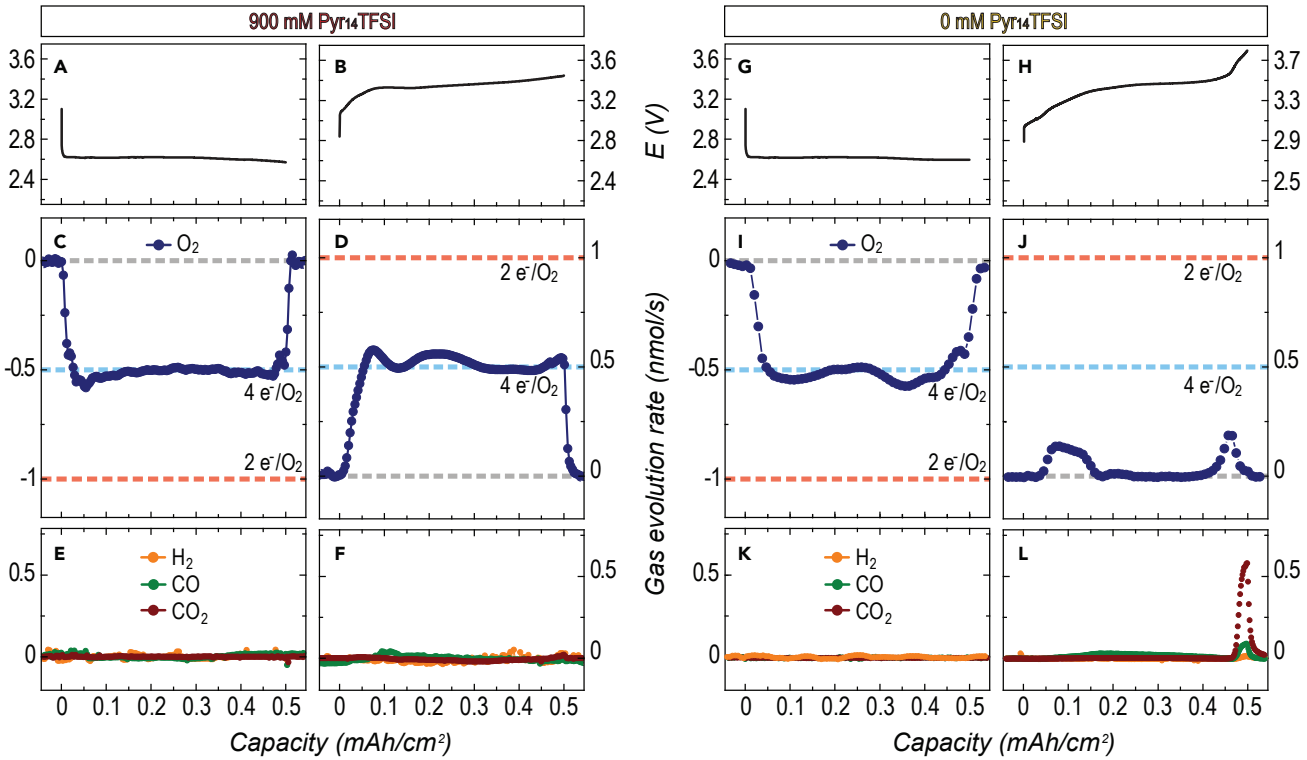

Figure 1. 4 e^-/O_2 Formation and Removal of LiOH in Water and IL-Containing Cells

(A, B, G, H) Galvanostatic profiles and (C, D, I, J) online mass spectrometry analysis of O_2, and (E, F, K, L) H_2, CO, and CO_2 (m/z = 32, 2, 28, 44, respectively) from batteries with electrolytes comprising of 700 mM LiTFSI, 50 mM LiI, and 5,000 ppm H_2O in G4 with 900 mM $Pyr_{14}TFSI$ (left) and without $Pyr_{14}TFSI$ (right) cycled at a current of 50 μA/cm^2.

known for promoting LiOH formation during the ORR (between 1,500 and 5,000 ppm).[11] Figure 1 (system description in Figure S1A) shows the electrochemical profile (Figures 1A and 1B) and gas evolution rate of O_2 (m/z = 32; Figures 1C and 1D), H_2, CO, and CO_2 (m/z = 2, 28, 44; Figures 1E and 1F) for the discharge and charge of this cell (Figures 1G–1M show similar results for a cell without $Pyr_{14}TFSI$ for comparison). The electrochemical discharge profile (Figure 1A) shows a sustained single discharge plateau at 2.6 V (versus Li/Li^+). The discharge produces a constant consumption rate of O_2 of ~0.51 nmol/s (Figure 1C), corresponding to a 4 e^-/O_2 stoichiometry, with no significant evolution of gases indicative of parasitic reactions (Figure 1E). The total measured O_2 consumption is 18.5 mmol, which corresponds to a 99.1% faradic efficiency.

The charge profile shows an initial rapid increase in potential from 3.1 to 3.3 V followed by a relatively flat process at approximately 3.4 V (Figure 1B). Notably, oxygen evolution is clearly observed to occur from the beginning of charge, stabilizing at around a rate corresponding to a 4 e^-/O_2 stoichiometry (Figure 1D). A total of 18.4 mmols of O_2 is evolved during charge, corresponding to 99.5% of the amount consumed in the discharge (i.e., a 99.5% faradic efficiency), with no significant signs of parasitic reactions as signaled by a lack of evolution of H_2, CO, or CO_2 (Figure 1F). The OER can be observed for several cycles (Figure S5) with a relatively high faradic efficiency (>80% for 7 cycles).

By comparison, in the absence of $Pyr_{14}TFSI$, only very small amounts of O_2 (1.5 mmols corresponding to ~8.4% faradic efficiency) (Figure 1K) are detected

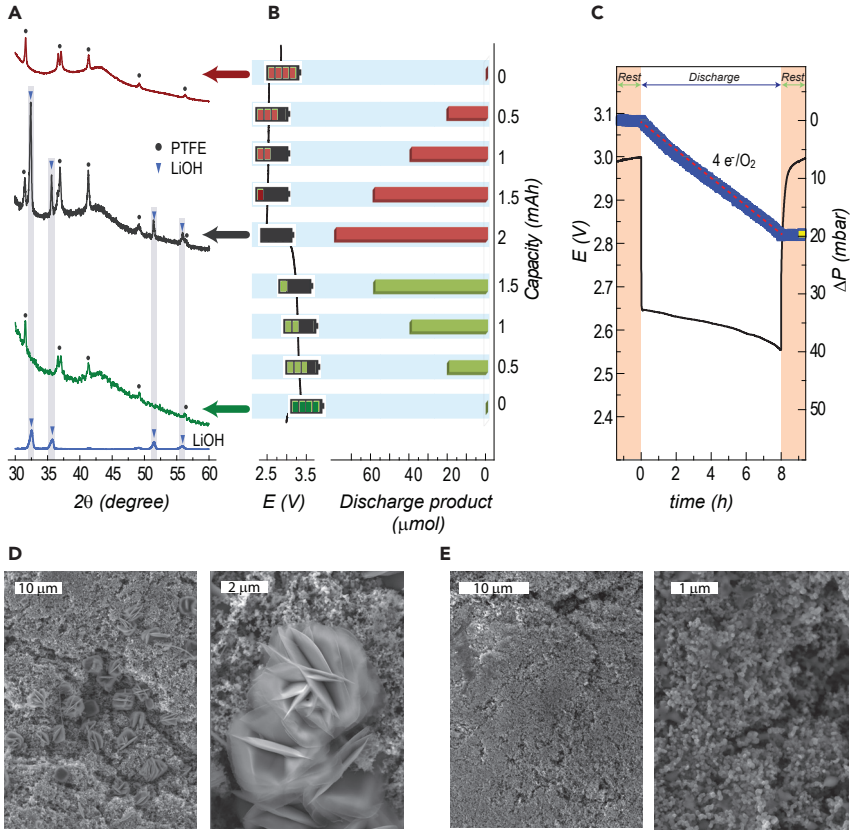

Figure 2. *Operando* and *Ex Situ* Characterization of the LiOH Formation during ORR

(A) X-ray diffractograms at different stages of capacity-limited cycling (pristine, red; discharged, gray; fully charged, green) as represented in the electrochemical profile.

(B) Quantification of LiOH present in the electrode by acid/base titration at different stages of capacity-limited cycling.

(C) *Operando* pressure-monitoring experiment during discharge.

(D and E) SEM characterization (at two different magnifications) of electrodes at the end of discharge (D) and end of charge (E) (scale bars shown in white).

Relevant reflections due to LiOH and PTFE binder are indicated by gray triangles and blue dots, respectively, in (A). All cells were cycled at 50 μA/cm^2.

during charge to 3.5 V. A steep increase in potential above 3.6 V at the end of charge is also observed, which is accompanied by a significant evolution of CO_2 (and O_2 and CO to lesser extent), suggesting electrode/electrolyte degradation (Figure 1M).

Analysis of the ORR Products

Analysis of the cathode after discharge with X-ray diffraction (XRD) (Figure 2A, gray trace) is dominated by patterns corresponding to crystalline LiOH, as revealed by quantitative analysis of the diffraction pattern (Figure S2). All reflections associated with LiOH are absent in the diffractogram of the fully charged electrodes, confirming the removal of the crystalline discharge product (Figure 2A, green trace). Quantification of the amount of LiOH present in the electrode was performed by acid titration at various stages of the discharge ($^1/_4$, $^1/_2$, $^3/_4$, and full discharge) and the charge ($^1/_4$, $^1/_2$, $^3/_4$, and full charge) processes. Figure 2B shows an increasing amount of LiOH detected in the electrode as the ORR progresses (red bars),which matches the expected value for a 1 e^-/LiOH mechanism (4 e^-/O_2) at all stages of discharge. The presence of Li_2O_2 as an alternative discharge product was also tested by iodometry

titration (Figure S3); no peroxide was detected, in agreement with the XRD analysis. A similar trend can be observed during different stages of the OER (Figure 2B, green bars), indicating that LiOH is being removed according to the same 1 e^-/LiOH stoichiometry. *Operando* pressure monitoring during discharge (Figure 2C) confirms a 4 e^-/O_2 stoichiometry during ORR for cells with 900 mM $Pyr_{14}TFSI$ and 5,000 ppm of water, as expected for the formation of LiOH. These results suggest that galvanostatic cycling of this cell occurs through the formation and removal of LiOH, and not through Li_2O_2 chemistry under the experimental conditions shown in Figure 1 (Figure S6).

Scanning electron microscopy (SEM) images of electrodes during the first discharge are shown in Figure 2D. The electrodes extracted from capacity-limited cells (2 mAh) discharged cells contain typical "flower-like" LiOH crystals of up to 7 μm in size, similar to those previously reported in cells containing LiI and water.[12] The absence of these crystalline structures in the SEM images of fully recharged electrodes (Figure 2E) confirms the removal of the discharge product during charge without the precipitation of large quantities of by-products from parasitic reactions. The consumption/regeneration of water, consistent with the reversible formation/decomposition of LiOH through the mechanism presented in Reaction 1, was also observed (Figure S7).

In order to evaluate the mechanistic implications of the observed stoichiometry during the OER in Figure 1, further OEMS experiments were performed with an electrochemically preloaded electrode with Li_2O_2 (Figure 3, left); the electrode was produced by discharging a cell using 300 mM LiTFSI in G4 as the electrolyte (i.e., with no LiI or additives). The cell was subsequently disassembled in the glove box, and the electrode was washed 3 times with ethylene glycol dimethyl ether (G1) and dried under vacuum for 30 min. This electrode was then loaded in a two-compartment cell with the same catholyte used for the cells shown in Figure 1 (i.e., 700 mM LiTFSI, 50 mM LiI, 900 mM $Pyr_{14}TFSI$, and 5,000 ppm H_2O in G4). In this case, the OER showed an approximately 2 e^-/O_2 stoichiometry (Figure 3C), consistent with the oxidation of Li_2O_2. After initially reaching an evolution rate corresponding to 2 e^-/O_2, a noticeable dip in the oxygen evolution is seen (Figure 3C). This effect has been previously attributed to a transition from the delithiation of Li-deficient ($Li_{2-x}O_2$) species to stoichiometric Li_2O_2 on Li_2O_2 particles.[38–40] Preloading was similarly performed using the IL-free conditions previously shown to produce LiOH electrochemically:[11] an electrolyte comprising 700 mM LiTFSI, 50 mM LiI, and 5,000 ppm H_2O in G4 was discharged. Switching to the IL-containing electrolyte resulted in 4e^-/O_2, OER on charge (Figure S12).

Since earlier ^{17}O-ssNMR measurements have reported that both O_2 and H_2O contribute to the oxygen atoms in the LiOH formed via a LiI-catalyzed electrochemical reaction in G1,[11] a further OEMS experiment was performed using ^{17}O-enriched H_2O (Figure 3, right) and $Pyr_{14}TFSI$. A m/z = 32 mass spectrometer signal (Figure 3D, blue) dominates the response on charge, which is due to ^{16}O-^{16}O. A signal is seen at m/z = 33 (Figure 3D, magenta), which corresponds to ^{17}O-^{16}O. The signal at m/z = 34 (Figure 3D, orange) corresponds to either ^{17}O-^{17}O or ^{18}O-^{16}O. Since the signal intensity of the m/z = 33 and 34 signals are similar in magnitude, this indicates that the m/z = 33 signal is not due to the ^{17}O in O_2 gas, since the natural abundance of ^{17}O and ^{18}O are 0.04% and 0.2%, respectively. The low enrichment of the $H_2{}^{17}O$ resulted in a relatively low Li^{17}OH concentration, as observed by ^{17}O ssNMR (Figure S13). This explains the relatively low intensity of the m/z = 33 signal (from ^{16}O-^{17}O) compared with the m/z = 32 signal (from ^{16}O-^{16}O).

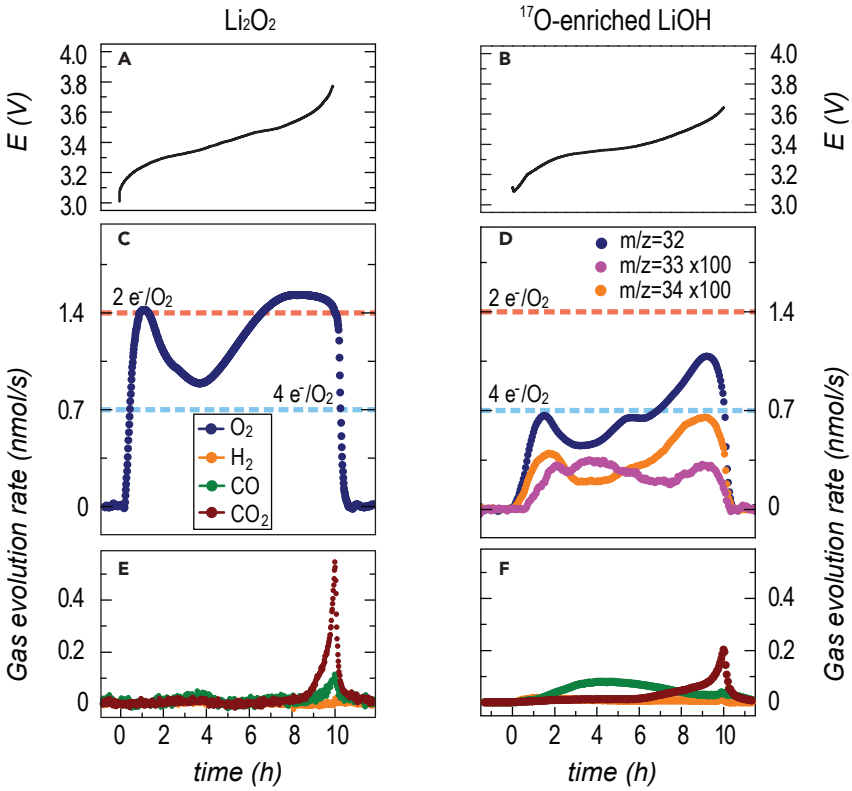

Figure 3. *Operando* Gas Analysis of Preloaded Electrodes and Isotopic Exchange during OER

(A and B) Galvanostatic profiles (top) and (C and D) online mass spectrometry analysis of O_2 (m/z = 32) and (E and F) H_2, CO, and CO_2 (m/z = 2, 28, 44) evolution during charge of electrochemically preloaded electrodes with Li_2O_2 (left) and of a Li-O_2 cell discharged using ^{17}O-enriched H_2O in the electrolyte containing G4 and $Pyr_{14}TFSI$ at 70 μA/cm^2.

Pathways to LiOH Removal

The mechanisms for LiOH formation in the ORR reaction have been discussed extensively elsewhere,[11,15,34] and thus we focus here on the OER reaction during charge (verification of the ORR mechanism is shown in Figure S14). Two questions arise from the OEMS data (Figure 1). First, what is the role played by $Pyr_{14}TFSI$ in the promotion of oxygen evolution? Second, what is the mechanism for LiOH decomposition/removal in the absence of the ionic liquid when there is no O_2 evolution?

The OER, during the charge of a LiOH-based Li-O_2 battery, can be described overall by:

$$4\ Li^+_{(sol)} + 4\ OH^-_{(sol)} \rightleftarrows 2\ H_2O_{(sol)} + O_{2(sol)} + 4\ Li_{(s)}. \qquad \text{(Reaction 1)}$$

However, this reaction operates via a two-stage catalytic mechanism in which I^- is first oxidized to I_3^- (the I^-/I_3^- couple, here referenced to the Li anode [the Li/Li^+ couple]),

$$2\ Li^+_{(sol)} + 3\ I^-_{(sol)} \rightleftarrows I_3^-{}_{(sol)} + 2\ Li_{(s)}, \qquad \text{(Reaction 2)}$$

and, subsequently, LiOH is oxidized to O_2 by I_3^- with the regeneration of I^- ($OH^- \rightarrow O_2$ chemical reaction):

$$4\ OH^-_{(sol)} + 2\ I_3^-{}_{(sol)} \rightleftarrows 6\ I^-_{(sol)} + 2\ H_2O_{(sol)} + O_{2(sol)}. \qquad \text{(Reaction 3)}$$

The (I^-/I_3^-) redox potential at standard (aqueous) conditions ($E^\circ_{versus\ Li/Li^+}$) corresponds to 3.5761 V,[18,41] which is sufficiently large to drive oxygen evolution. However, the reversibility of iodide-mediated aprotic Li-O_2 batteries, cycling through LiOH, has been a much-discussed subject due to the difficulty of performing the OER process at low overpotentials (below 3.5 V).[14–17,19] Alternative reaction pathways have therefore been proposed in the literature to explain the LiOH removal upon charging in LiI- and organic-electrolyte-containing cells with added water. The detection of IO_3^- in the electrolyte of charged cells, alongside the lack of O_2 evolution in OEMS experiments, has suggested that IO_3^- is the dominant product rather than O_2 at 3.5 V or below, in ether-based electrolytes. The IO_3^- formation has been proposed to form either through the oxidation of I^- to I_2

$$2\ I^- \rightleftarrows I_2 + 2\ e^- \qquad \text{(Reaction 4)}$$

and its subsequent chemical reaction with LiOH[14,15]:

$$3\ I_2 + 6\ OH^- \rightleftarrows IO_3^- + 5\ I^- + 3\ H_2O \qquad \text{(Reaction 5)}$$

or via oxidation by I_3^- to form IO^- and the subsequent disproportionation of IO^- into IO_3^- and I^-[18,42]:

$$6\ OH^- + 3\ I_3^- \rightleftarrows 8\ I^- + 3\ H_2O + IO_3^-. \qquad \text{(Reaction 6)}$$

In this study, cells containing $Pyr_{14}TFSI$ show clear evidence for a 4 e^-/O_2 OER (Reaction 1) commencing at ~3.2 V (Figures 1A–1F). This oxygen evolution is absent in cells without the IL (Figures 1G–1M), even when charging at comparable potentials (below 3.5 V for ~75% of charge).

Characterization of the electrolyte after charge was performed in order to establish the products formed following LiOH removal in cells with and without IL and thus investigate the difference in mechanism during the OER. UV spectra of aliquots of the electrolyte of charged cells with and without $Pyr_{14}TFSI$ (Figure 4A) show the presence of features at 295 and 354 nm, corresponding to the presence of I_3^-; no feature corresponding to I_2 (at 520 nm) is seen in either case (insert in Figure 4A). The electrolyte of cells without $Pyr_{14}TFSI$ (Figure 4A, red trace) show the presence of extra features at 228 and 465 nm, assigned to IO_3^- and IO^-, respectively; these are absent in cells cycled with the IL (Figure 4A, blue trace). The presence of I_3^- in both samples indicates that this is the main product of I^- oxidation and therefore suggests that this is the species responsible for oxidizing LiOH, rather than I_2. The lack of O_2 evolution observed in OER data of cells without $Pyr_{14}TFSI$ can therefore be explained by the formation of oxidized iodine species (IO^- and IO_3^-), the oxygen effectively being trapped in the solution, as previously reported for similar electrolytes.[14–16]

The capability of I_3^- to oxidize LiOH during the OER was subsequently tested. A solution of I_3^- was injected into a mixture of electrolyte containing 700 mM LiTFSI, 50 mM LiI, 900 mM $Pyr_{14}TFSI$, and 5,000 ppm H_2O in G4, and commercial LiOH powder. The subsequent gas evolution was measured by mass spectrometry (Figure 4B). Gas evolution from the LiOH powder, at m/z = 32, can be directly observed as soon as the I_3^- solution is injected, confirming the evolution of O_2 from this mixture and demonstrating that I_3^- is capable of oxidizing LiOH in this electrolyte; very little O_2 evolution is observed in the absence of $Pyr_{14}TFSI$.

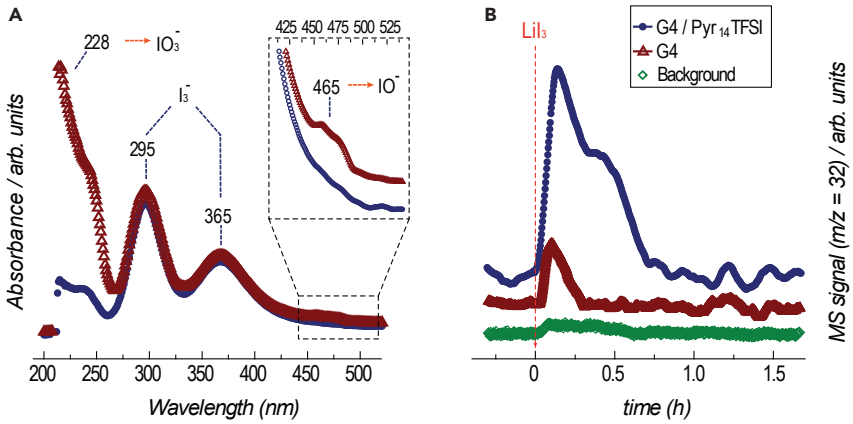

Figure 4. Spectroscopic and Electrochemical Analysis of the I_3^- Oxidizing Power

(A) UV spectra of catholytes collected after galvanostatic discharge and charge of cells containing 700 mM LiTFSI, 50 mM LiI, and 5,000 ppm H_2O (red trace) and with 900 mM $Pyr_{14}TFSI$ (blue trace) in G4.

(B) Online mass spectrometry test of the reaction of I_3^- with LiOH. A 50 mM I_3^- solution is injected into a vessel containing LiOH powder immersed in electrolyte with 700 mM LiTFSI, 50 mM LiI, 900 mM $Pyr_{14}TFSI$, and 5,000 ppm H_2O in G4 (blue trace) and 700 mM LiTFSI, 50 mM LiI, and 5,000 ppm H_2O in G4 (red trace). The gas evolution of the ensuing reaction was recorded with a mass spectrometer (m/z = 32, corresponding to O_2 evolution is displayed). A blank spectrum was collected by injecting the I_3^- solution into the electrolyte containing 700 mM LiTFSI, 50 mM LiI, 900 mM $Pyr_{14}TFSI$, and 5,000 ppm H_2O in G4 in the absence of LiOH (green trace). Argon was used as the carrier gas.

In order to assess the thermodynamic consistency of this reaction pathway, and whether the I^-/I_3^- couple provides a sufficient driving force for the OER, the Gibbs free energy of the OER ($\Delta_{OER}G$) was estimated according to Reaction 1:

$$\Delta_{OER}G = 2\Delta_fG^\circ(H_2O) + \Delta_fG^\circ(O_2) + 4\Delta_fG^\circ(Li) - 4\Delta_fG^\circ(OH^-) - 4\Delta_fG^\circ(Li^+) + 2\Delta_{sol}G(H_2O) + \Delta_{sol}G(O_2) - 4\Delta_{sol}G(OH^-) - 4\Delta_{sol}G(Li^+) \quad \text{(Equation 1)}$$

The $\Delta_{OER}G$ can then be written as the combination of Reactions 2 and 3 (the (I^-/I_3^-) redox pair, and the $OH^- \rightarrow O_2$ chemical reaction, respectively), giving the Gibbs free energy

$$\Delta_{OER}G = 2\Delta_rG(I^-/I_3^-) + \Delta_rG(OH^- \rightarrow O_2), \quad \text{(Equation 2)}$$

where $\Delta_rG(I^-/I_3^-)$ is the Gibbs free energy of the I^-/I_3^- redox couple, defined as

$$\Delta_rG(I^-/I_3^-) = \Delta_fG^\circ(I_3^-) + 2\Delta_fG^\circ(Li) - 2\Delta_fG^\circ(Li^+) - 3\Delta_fG^\circ(I^-) + \Delta_{sol}G(I_3^-) - 2\Delta_{sol}G(Li^+) - 3\Delta_{sol}G(I^-), \quad \text{(Equation 3)}$$

and $\Delta_rG(OH^- \rightarrow O_2)$ is the Gibbs free energy of the $OH^- \rightarrow O_2$ chemical reaction, defined as

$$\Delta_rG(OH^- \rightarrow O_2) = 6\Delta_fG^\circ(I^-) + 2\Delta_fG^\circ(H_2O) + \Delta_fG^\circ(O_2) - 4\Delta_fG^\circ(OH^-) - 2\Delta_fG^\circ(I_3^-) + 6\Delta_{sol}G(I^-) + 2\Delta_{sol}G(H_2O) + \Delta_{sol}G(O_2) - 4\Delta_{sol}G(OH^-) - 2\Delta_{sol}G(I_3^-). \quad \text{(Equation 4)}$$

$\Delta_{OER}G$ depends on the Gibbs free energy of formation of H_2O ($\Delta_fG^\circ(H_2O)$), O_2 ($\Delta_fG^\circ(O_2)$), Li ($\Delta_fG^\circ(Li)$), OH^- ($\Delta_fG(OH^-)$), and Li^+ ($\Delta_fG^\circ(Li^+)$) at standard conditions, and their Gibbs free energy of solvation, ($\Delta_{sol}G(H_2O)$, $\Delta_{sol}G(O_2)$, $\Delta_{sol}G(Li)$, $\Delta_{sol}G(OH^-)$, and $\Delta_{sol}G(Li^+)$), which are solvent specific. $\Delta_fG^\circ(H_2O)$ and $\Delta_fG^\circ(O_2)$ are tabulated values,[41] whereas, by definition, $\Delta_fG^\circ(Li) = 0$. Using the Nernst

equation for the I^-/I_3^- redox couple, and assuming that the dissolved oxygen ($O_{2(sol)}$) is at equilibrium with oxygen gas ($O_{2(g)}$) at a pressure (P_{O_2}) and that the oxygen can be treated as an ideal gas over the range of temperature concerned (see Supplemental Information), the above expression can be written as:

$$\Delta_r G(OH^- \rightarrow O_2) = 2\Delta_f G^\circ(H_2O) - 4\Delta_f G^\circ(LiOH) + 2nFE\left(I^-/I_3^-\right) + 2\Delta_{sol}G(H_2O) + kT\ln\left(\frac{P_{O_2}}{P^\circ}\right). \quad \text{(Equation 5)}$$

This expression indicates that three key variables dictate the driving force for the OER: the redox equilibrium potential of the I^-/I_3^- couple ($E(I^-/I_3^-)$), the water activity ($\Delta_{sol}G(H_2O)$), and the oxygen partial pressure (P_{O_2}). The redox potential of the iodide/triiodide redox system is solvent dependent,[18–20] the couple varying by over 0.5 V,[18] whereas variations in the solvent activity and gas partial pressure are of smaller magnitude (estimated to be ~0.17 and ~0.08 eV, respectively; Table S2). The variability in the values of the $E(I^-/I_3^-)$ is strongly influenced by stabilizing (donor-acceptor) interactions of I^- species in solution,[18,20] since $\Delta_r G(I^-/I_3^-)$ is proportional to the difference in $\Delta_{sol}G$ of I^- and I_3^-:

$$\Delta_r G\left(I^-/I_3^-\right) \propto \Delta_{sol}G\left(I_3^-\right) - 3\Delta_{sol}G(I^-) \quad \text{(Equation 6)}$$

The OEMS results presented in Figures 1, 3, and 4 suggest that the addition of $Pyr_{14}TFSI$ (alongside small amounts of water) is capable of increasing the oxidizing power of I_3^- and/or reducing the couple of the OER sufficiently so that it can occur below 3.5 V. We now turn to identify and rationalize the effect of the additives (water, IL) on the redox equilibrium potential of the I^-/I_3^- couple.

Modification of the I^-/I_3^- Redox Potential

Effect of the Additives on the Coordination of I^- and on the OER. It has recently been shown that water and ILs are among the media in which $E(I^-/I_3^-)$ has the highest values, due to the very strong coordination of I^- by these solvent molecules:[18] water molecules, for example, solvating I^- ions via hydrogen-halogen bonds within the I^- first solvation shell. In order to investigate the effect of the additives used here, we have explored potential correlations between the ^{1}H-NMR chemical shift of the water peak and the I^-/I_3^- redox potential (Figure 5). The addition of 5,000 ppm of water to an electrolyte with no IL (700 mM LiTFSI, 50 mM LiI in G4) increases $E(I^-/I_3^-)$ by only ~0.01 V (Figure 5D). ^{1}H-NMR spectra of the same electrolyte with increasing amounts of water (Figure 5F) are consistent with prior work:[11] at low water concentrations, a peak is observed at high frequencies, consistent with strong H_2O:I^- interactions. The chemical shift is slightly lower than that of bulk water, as this effect is less significant than the shift arising from H-bonding interactions between water molecules. As the water concentration increases for a fixed LiI content, the peak shifts from 4.45 to 4.35 ppm again indicating weaker H_2O:I^- interactions. In previous work,[11] the trend was then seen to reverse at higher water concentrations of >5% H_2O (and 50 mM LiI) due to the strong hydrogen bonding interactions in between molecules in water clusters, resulting in a shift toward the position of bulk water.

The progressive addition of $Pyr_{14}TFSI$ to the electrolyte containing 5,000 ppm of water (700 mM LiTFSI, 50 mM LiI in G4) shows a similar trend in the ^{1}H-NMR spectra (Figures 5A, 5B, and S16), with the water peak shifting downfield even further from 4.35 to 4.1 ppm on addition of 900 mM $Pyr_{14}TFSI$, suggesting either reduced H_2O:I^- interactions and/or reduced H_2O H-bonding. In both scenarios, this indicates an increased "solvation" of the water and I^- by the IL. This increase in $Pyr_{14}TFSI$ concentration also has a large associated increase in the I^-/I_3^- redox potential, from

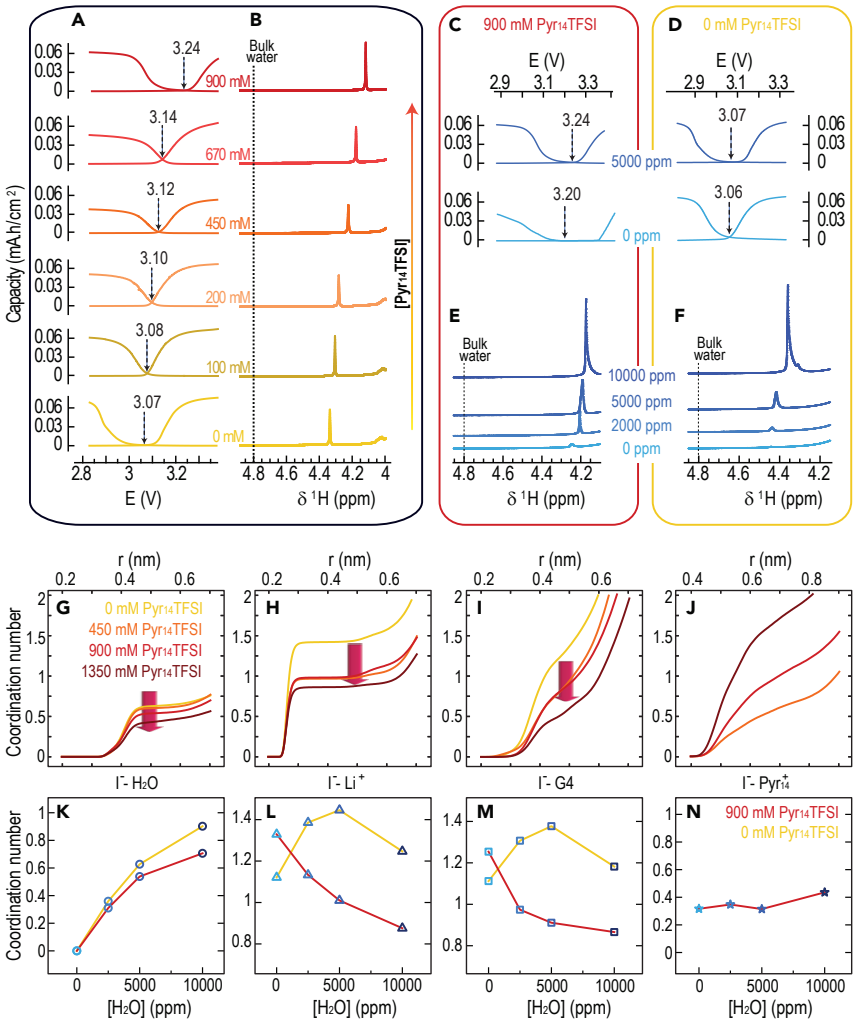

Figure 5. Correlation between Water Chemical Shift and I^-/I_3^- Equilibrium Redox Potential

(A and B) Effect of $Pyr_{14}TFSI$ concentration (0 – 900 mM) on (A) galvanostatic charge-discharge curves, and (B) solution ^{1}H-NMR of 700 mM LiTFSI, 50 mM LiI, and 5,000 ppm H_2O in G4 electrolyte.

(C and D) Effect of water concentration (0 versus 5,000 ppm) on galvanostatic charge-discharge curves of electrolytes with (C) 900 mM and (D) 0 mM $Pyr_{14}TFSI$.

(E and F) Solution ^{1}H-NMR of electrolytes with increasing amounts of water with (E) 900 mM and (F) 0 mM $Pyr_{14}TFSI$.

(G–J) MD coordination number (CN) plots of the I^- center of mass to (G) H_2O, (H) Li^+, (I) G4, and (J) Pyr_{14}^+ as a function of distance for 5,000 ppm H_2O in 700 mM LiTFSI, 50 mM LiI, in G4 electrolyte with increasing amounts of $Pyr_{14}TFSI$ (0–1,350 mM).

(K–N) Evolution of the I^- CN in the first coordination shell to (K) H_2O, (L) Li^+, (M) G4, and (N) Pyr_{14}^+ (measured at 0.5 nm for H_2O, Li^+, and G4 and at 0.7 nm for Pyr_{14}^+) as a function of [H_2O] in electrolytes with 0 mM $Pyr_{14}TFSI$ (yellow lines) and 900 mM $Pyr_{14}TFSI$ (red lines). All galvanostatic cycling was performed at 50 μA/cm^2 under argon in cells containing a LICGC. 300 mM LiTFSI in G4 was used as the anolyte.

3.07 to 3.24 V (~0.17 V), consistent with the strong interaction between I^- and Pyr_{14}^+ (also shown in CV data in Figure S15). The largest value of $E(I^-/I_3^-)$ is observed when $Pyr_{14}TFSI$ is present, the effect on the I^-/I_3^- coupling of adding Pyr_{14}^+ being stronger than the addition of 5,000 ppm of water as shown in Figures 5C and 5D. A smaller shift in the ^{1}H resonance is observed upon increasing water concentration (between 2,000 and 5,000 ppm) in the presence of $Pyr_{14}TFSI$ ($\Delta\delta = -0.03$ ppm; Figure 5E) than

in its absence ($\Delta\delta$ = −0.08 ppm; Figure 5F), which is indicative of weaker water-I^- interactions in the presence of the IL. This reduced water-I^- interaction and the higher measured $E(I^-/I_3^-)$ suggest that the Pyr_{14}^+ cation may be a stronger coordinating agent for I^- ions than water under the conditions used here. The larger ^1H shifts of the water peak observed in pure $Pyr_{14}TFSI$, compared to the mixtures shown in Figure 5 (Figure S17), is in agreement with a synergistic coordination effect of both water and $Pyr_{14}TFSI$ toward I^-. This is in agreement with the hard and soft acids and bases (HSAB) concept,[42] since the introduction of the Pyr_{14}^+ cation, a softer Lewis base than Li^+ and H^+ (the other cations present in the electrolyte), would be expected to have a strong impact on the coordination of I^-, which is a soft Lewis acid.

In order to investigate the effects of the additives on the coordination of I^-, MD simulations were performed. Figures 5G–5L show the average coordination number (CN) of I^- to different species as a function of distance. The increase in $Pyr_{14}TFSI$ concentration reduces the contributions in the first I^- coordination shell from H_2O (Figure 5G), Li^+ (Figure 5H), and G4 (Figure 5K), while the contribution from Pyr_{14}^+ increases (Figure 5L). The MD results are consistent with the ^1H-NMR results, the increase in the H_2O molecules in the first coordination shell of I^- with increasing water concentration (Figure 5M) correlating with the shift of the water ^1H-NMR peak to lower values in both the absence (Figure 5F) and the presence of the IL (Figure 5E). The smaller chemical shift of the ^1H-NMR water peak observed in the presence of $Pyr_{14}TFSI$ is correlated with a smaller increase of H_2O molecules in the first coordination shell of I^- (Figure 5M). This effect has further implications on the coordination of I^- by Li^+ and G4: the number of I^--Li^+ (Figure 5H) and G4-I^- (Figure 5K) interactions in the first coordination shell of I^- decreases with increasing water content (up to 5,000 ppm) in the absence of IL. However, the presence of IL (900 mM) reverses this effect, and both Li^+ (Figure 5H) and G4 (Figure 5K) are on average increasingly present in the first coordination shell of I^- with increasing water content. This indicates a fundamentally different contribution of the IL to the solvation of I^- compared to water and corroborates the complex interplay between the two additives used in the electrolyte capable of undergoing OER during LiOH oxidation (Figure 1).

The disruptive insertion of Pyr_{14}^+ ions into the first coordination shell of I^- can be clearly visualized in snapshots of the final state of the simulations of electrolytes with increasing $Pyr_{14}TFSI$ concentrations shown in Figures 6A–6D. The comparative levels of coordination of Li^+, H_2O, G4, and Pyr_{14}^+ ions, evaluated as a function of the concentration of $Pyr_{14}TFSI$ (Figure 6E), indicate a strong Pyr_{14}^+-I^- interaction, to levels comparable to that of Li^+ and H_2O at [$Pyr_{14}TFSI$] = 900 mM, in agreement with previous MD studies.[16,18] This complex interplay is also reflected on the mobility of I^- ions (their mean squared displacement) in the electrolyte (Figure 6F). In the absence of IL, I^- mobility is not strongly affected by increasing amounts of water (solid lines) up to 10,000 ppm. The presence of 900 mM of $Pyr_{14}TFSI$ in neat electrolytes reduces I^- ion mobility compared to the electrolyte with no IL (light blue traces). However, the presence of $Pyr_{14}TFSI$ has the effect of substantially increasing I^- ion mobility with increasing water content up to 5,000 ppm. At higher water content, the mobility is reduced to some extent due to the onset of water clusters formation.[11] The electrolyte mixture used in the cell reported in Figure 1 (900 mM $Pyr_{14}TFSI$ and 5,000 ppm of water) has similar average amounts of Li^+, G4, and Pyr_{14}^+ in the first coordination shell of I^- (Figure 6E), and it has the highest measured I^- mobility (Figure 6F).

Thermodynamic Analysis of the Effect of Additives. The measurements of the I^-/I_3^- redox potential shown in Figure 5A allow us to estimate the effect of the additives

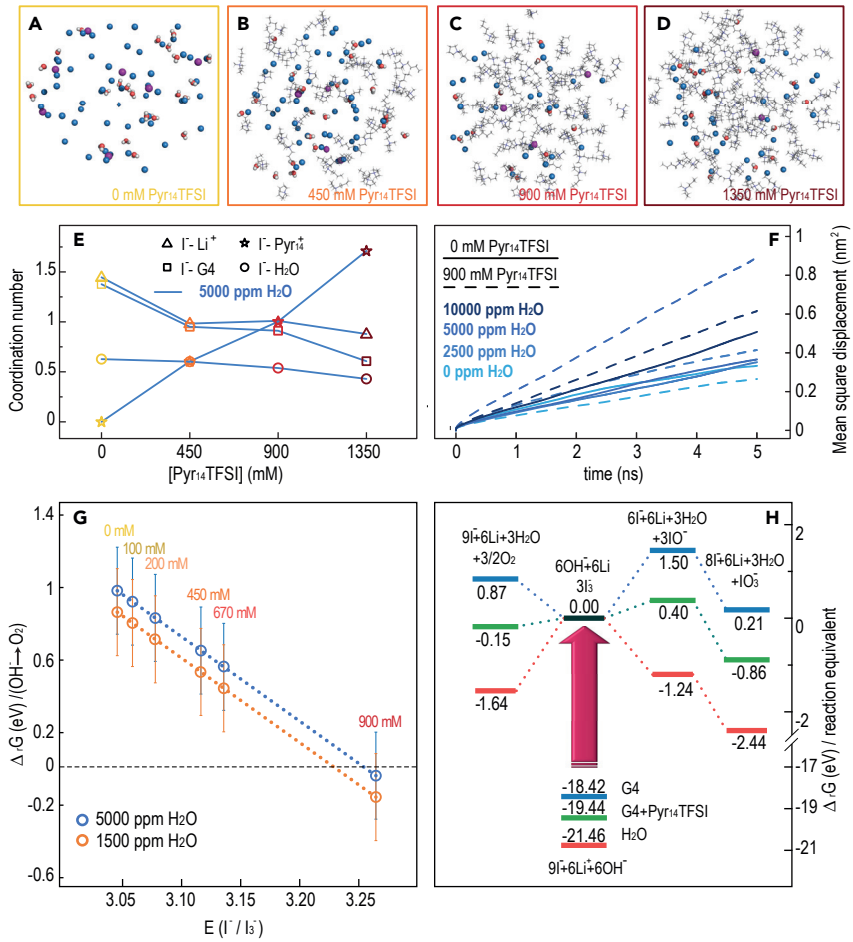

Figure 6. MD Simulations of Electrolytes with Varying Levels of Additives; Implications for the Thermodynamic Drive for the OER

(A–D) Snapshots of the final state of the simulations of electrolytes containing 700 mM LiTFSI, 50 mM LiI, and 5,000 ppm H_2O in G4 with (A) 0 mM, (B) 450 mM, (C) 900 mM, and (D) 1,200 mM $Pyr_{14}TFSI$ showing I^- (magenta), Li^+ (blue), H_2O (red/white), and Pyr_{14}^+ (sticks). G4 molecules are omitted for clarity.

(E) Plot of the evolution of the CN in the first coordination shell of I^- to H_2O, Li^+, G4, and Pyr_{14}^+ with increasing $Pyr_{14}TFSI$ concentration in electrolytes containing 5,000 ppm H_2O.

(F) Mean square displacement of I^- ions in electrolytes with 0 mM $Pyr_{14}TFSI$ (solid lines) and 900 mM $Pyr_{14}TFSI$ (dashed lines) with increasing water concentration.

(G) Effect of the various $E(I^-/I_3^-)$ couples measured for different $Pyr_{14}TFSI$ concentrations (shown in Figure 5A) on the thermodynamic driving force for the OER, assuming 5,000 ppm (end of charge, blue) and 1,500 ppm of water (beginning of charge, orange). The error bars are calculated based on the assumptions made in the calculations (see Supplemental Information).

(H) Free-energy diagram for the proposed mechanisms involving the iodide-mediated LiOH oxidation (O_2 evolution [left], IO^- and IO_3^- formation [right], relative to I_3^- formation in G4 [blue], G4 + 900 mM $Pyr_{14}TFSI$ [green], and H_2O [red]). The Gibbs free-energy values were calculated for the electrolytes containing 700 mM LiTFSI, 50 mM LiI, and 5,000 ppm H_2O in G4 with 0 mM and 900 mM $Pyr_{14}TFSI$ ($E(I^-/I_3^-)$ = 3.07 V and 3.24 V, respectively; Figure 5A) and in standard conditions. All electrochemical reactions are scaled to 6 e^- so as to compare the free energies of the various reactions.

used in this work on the thermodynamic drive of the OER using Equation 5. Figure 6G shows an estimation of $\Delta_r G(OH^- \rightarrow O_2)$ as a function of the I^-/I_3^- redox potential in electrolyte mixtures with increasing $Pyr_{14}TFSI$ concentration for two levels of H_2O concentration (1,500 ppm [orange] and 5,000 ppm [blue], representing the theoretical levels at the beginning and end of the charge, respectively). The calculation of

the thermodynamic drive of the OER has been scaled up to $6e^-$ (instead of the $4e^-$ process described above) in order to allow direct comparison with the formation of IO^- and IO_3^- (Figure 6H). It can be seen that only at a I^-/I_3^- redox potential above ~3.24 V does the OER becomes thermodynamically favorable, with $\Delta_r G(OH^- \rightarrow O_2) \approx -0.03$ eV (± 0.24) for [$Pyr_{14}TFSI$] = 900 mM at 5,000 ppm H_2O and ≈ -0.15 eV (± 0.24) at 1,500 ppm H_2O (see Supplemental Information for details). These values are very close to, or below, zero at equilibrium conditions, within the error margins arising from the assumptions made in the calculations and the measurement limitations, and thus this process is energetically feasible considering the experimental conditions (see Tables S1–S4 and Figure S22). It is of course important to note that during the charge the cell is working under non-equilibrium conditions, where the [I_3^-] is higher and [I^-] lower than under equilibrium conditions, providing an additional driving the force for the OER. The high values of $E(I^-/I_3^-)$ observed in the electrolytes containing $Pyr_{14}TFSI$ and water can therefore provide a rationale for the observation of O_2 evolution during the charge process shown in Figures 1A–1F.

OER versus IO_3^- Formation

Our results (Figure 1) indicate that there is a very fine balance between the production of $LiIO_3$ and O_2, which we now discuss. The ability of I_3^- to oxidize LiOH to form $LiIO_3$ (via Reactions 5 and 6) has been found to be dependent on the Gutmann acceptor number (AN) of the solvent used, with I_3^- in N,N-dimethylacetamide (DMA), dimethyl sulfoxide (DMSO), and 1-methylimidazole (Me-Im) being capable of oxidizing LiOH (for AN > 13.6), but I_3^- in G1, G4, and pyridine being unable to.[19] In the absence of water, a LiI-containing electrolyte in diethylene glycol dimethyl ether (G2) requires potentials above the I_3^-/I_2 to remove LiOH from preloaded electrodes,[19] whereas the formation of IO_3^- was reported in a LiOH-saturated G1-based electrolyte containing water (3 wt%).[11,43] Electrochemically, several groups have reported the formation of IO^-/IO_3^- during the charge of LiOH-based Li-O_2 cells in glyme electrolytes containing water and iodide,[12,14,15,43] whereas in the absence of water, a charging plateau above the I_3^-/I_2 redox transition was reportedly required in G2[19] (Figure S21). Our studies clearly show that the addition of small quantities of water increases the I_3^- oxidative power and that it can oxidize LiOH under these conditions: during galvanostatic charge of cells with 50 mM LiI and 5,000 ppm H_2O in G4 (Figures 1G–1M), the charge process is observed to commence below the I_3^-/I_2 transition (from as low as 3.2 V). The detection of IO^- and IO_3^- in the UV spectra (Figure 4A) is therefore consistent with LiOH removal via Reactions 5 and 6.

It has recently been argued that $LiIO_3$ is the thermodynamic product, rather than O_2, on oxidation of Li_2O_2 by I_3^-, even though O_2 evolution is seen. The reported lack of $LiIO_3$ formation was ascribed in this study to the slow kinetics of O-O dissociation needed to form IO^- (and subsequently $LiIO_3$), even in solvents with low Gutmann AN, such as G4, where the decomposition of Li_2O_2 is very slow.[19] The authors similarly argued that the most thermodynamically favorable route for the oxidation of LiOH occurs through the formation of $LiIO_3$ (Reactions 5 and 6) rather than the formation of O_2 (Reaction 2). Our results motivate the same question as raised previously for O_2 evolution from Li_2O_2 in the presence of LiI: the presence of $Pyr_{14}TFSI$ increases the oxidizing power of I_3^- so that it can promote O_2 evolution, but why does it also disfavor the IO_3^- formation mechanism?

We now consider the thermodynamic driving force to form lithium iodate (IO_3^-) in basic media via an analogous analysis to the LiOH oxidation, through the I^--mediated OER described above. Starting with the following reaction (full derivation is found in the Supplemental Information):

$$6\,Li^{+}_{(sol)} + 6\,OH^{-}_{(sol)} + I^{-}_{(sol)} \rightleftarrows 3\,H_2O_{(sol)} + IO_3^{-}{}_{(sol)} + 6\,Li_{(s)}. \quad \text{(Reaction 7)}$$

This reaction is in fact redox mediated via the following two-stage catalytic mechanism in which I^- is first oxidized to I_3^- (I^-/I_3^- couple, Gibbs free energy: $\Delta_rG(I^-/I_3^-)$; Reaction 2). Subsequently, LiOH reacts chemically with I_3^- to form IO^- and H_2O (Gibbs free energy: $\Delta_rG(OH^- \rightarrow IO^-)$):

$$2\,OH^{-}_{(sol)} + I_3^{-}{}_{(sol)} \rightleftarrows I^{-}_{(sol)} + H_2O_{(sol)} + IO^{-}_{(sol)}. \quad \text{(Reaction 8)}$$

Finally, IO^- disproportionates to form IO_3^- and I^- (Gibbs free energy: $\Delta_rG(IO^- \rightarrow IO_3^-)$):

$$3\,IO^{-}_{(sol)} \rightleftarrows 2\,I^{-}_{(sol)} + IO_3^{-}{}_{(sol)}. \quad \text{(Reaction 9)}$$

The Gibbs free energy of IO_3^- formation ($\Delta_rG(OH^- \rightarrow IO_3^-)$) can therefore be calculated from the combination of the Gibbs free energy of these three reactions:

$$\Delta_rG\left(OH^- \rightarrow IO_3^-\right) = 3\Delta_rG'\left(I^-/I_3^-\right) + \Delta_rG(OH^- \rightarrow IO^-) + \Delta_rG\left(IO^- \rightarrow IO_3^-\right). \quad \text{(Equation 7)}$$

The key step in the IO^-/IO_3^- route during charge is the reaction of I_3^- and OH^- to form IO^- (Reaction 8), as this reversible process is directly in competition with the OER. While the formation of IO_3^- is thermodynamically downhill with respect to IO^-, the proposed mechanisms require the formation of IO^- as an initial step. As previously discussed, the solvation of I^- strongly influences the I^-/I_3^- redox potential, and therefore also $\Delta_rG(OH^- \rightarrow IO^-)$. However, the (formally) I^+ ion in I_3^- is consumed to create IO^-, generating only two I^- ions (Reaction 8), as opposed to three I^- ions in the OER reaction (Reaction 3). The effect of this difference, and whether this is sufficient to create a thermodynamic driving force for IO^- over O_2 because of it, can be assessed by examining the overall reaction to form IO^- (Reaction 8 + Reaction 2).

$$2\,Li^{+}_{(sol)} + 2\,OH^{-}_{(sol)} + I^{-}_{(sol)} \rightleftarrows 2\,Li_{(s)} + H_2O_{(sol)} + IO^{-}_{(sol)}, \quad \text{(Reaction 10)}$$

which competes with the formation of O_2 via the OER given in Reaction 1. The competition between these two reactions is described via the following equilibrium:

$$3\,I^{-}_{(sol)} + 3/2\,O_{2\,(sol)} \rightleftarrows 3\,IO^{-}_{(sol)}. \quad \text{(Reaction 11)}$$

The Gibbs free energy for this process can be calculated:

$$\Delta_rG(OH^- \rightarrow IO^-) - \frac{3}{2}\Delta_rG(OH^- \rightarrow O_2) = 0.40 + 3\Delta_{sol}G(IO^-) - 3\Delta_{sol}G(I^-) - \frac{3}{2}kT\ln\left(\frac{P_{O_2}}{P^{\circ}}\right). \quad \text{(Equation 8)}$$

This indicates that, under standard conditions (implying Δ_{sol} terms are 0), the thermodynamic drive for the OER versus IO^- formation is +0.40 eV (as $3\Delta_fG(IO^-) - 3\Delta_fG(I^-)$ = +0.40 eV from Equation 8; see Supplemental Information).[41] However, the thermodynamic drive is solvent dependent due to differences in solvation energies of I^-, IO^-, and O_2 (Equation 8). If the value of $\Delta_{sol}G(O_2)$ is assumed to be unchanging in the various electrolytes under consideration, then the thermodynamic balance between the formation of IO^- and O_2 ($\Delta_rG(OH^- \rightarrow IO^-) - \Delta_rG(OH^- \rightarrow O_2)$) hinges entirely upon the difference in the Gibbs free energy of solvation of I^- and IO^- in different electrolytes ($\Delta_{sol}G(IO^-) - \Delta_{sol}G(I^-)$).

To obtain an understanding of the magnitude of the solvation energy terms, density functional theory (DFT) calculations with implicit solvation were performed (see Supplemental Information). The calculated difference in the Gibbs free energy of solvation of I^- and IO^- ($3\Delta_{sol}G(IO^-) - 3\Delta_{sol}G(I^-)$) is +0.22 eV in G4 and +0.15 eV in pure $Pyr_{14}TFSI$, making $\Delta_rG(OH^- \rightarrow IO^-) - \frac{3}{2}\Delta_rG(OH^- \rightarrow O_2)$ +0.63 eV and +0.55 eV in G4 and pure $Pyr_{14}TFSI$, respectively; i.e., the formation of IO^- is thermodynamically unfavorable in comparison to the OER regardless of the presence or absence of IL.

A similar thermodynamic analysis of the formation of IO_3^- can be performed (see Supplemental Information):

$$\Delta_rG\left(OH^- \rightarrow IO_3^-\right) - \frac{3}{2}\Delta_rG(OH^- \rightarrow O_2) = -0.79 + \Delta_{sol}G\left(IO_3^-\right) - \Delta_{sol}G(I^-) - \frac{3}{2}kT\ln\left(\frac{P_{O_2}}{P^\circ}\right). \quad \text{(Equation 9)}$$

The formation of IO_3^- is more thermodynamically favorable than the OER under standard conditions (−0.79 eV),[41] and the thermodynamic balance between the formation of IO_3^- and O_2 in different electrolytes again depends on ($\Delta_{sol}G(IO_3^-) - \Delta_{sol}G(I^-)$). DFT calculations similarly show that the solvation of IO_3^- in G4 and $Pyr_{14}TFSI$ is less favorable than that in water by amounts very similar to those found for IO^- and I^- ($\Delta_{sol}G\left(IO_3^-\right)$ = +0.44 and +0.28 eV, respectively). This results in the difference in driving force for the formation of IO_3^- over O_2 (Equation 9) being reduced to −0.627 eV and −0.557 eV in G4 and pure $Pyr_{14}TFSI$, respectively; i.e., IO_3^- formation is always favored over the OER in all solvents.

Figure 6H shows free energy diagrams comparing the thermodynamic drive to form O_2 (Equation 5) versus IO^- (Equation 8) and IO_3^- (Equation 9) in electrolytes with and without IL, and in standard conditions. The value of $E(I^-/I_3^-)$ used for the calculations is the one measured for the electrolytes containing 700 mM LiTFSI, 50 mM LiI, and 5,000 ppm H_2O in G4 with 0 mM and 900 mM $Pyr_{14}TFSI$ ($E(I^-/I_3^-)$ = 3.07 V and 3.24 V, respectively; Figure 5A), while the solvation energy terms were calculated for implicit solvents (in pure G4, $Pyr_{14}TFSI$, and water, respectively). The overall thermodynamic analysis indicates that the introduction of $Pyr_{14}TFSI$ (Figure 6H) to G4 has two effects: (1) oxidation of OH^- by I_3^- becomes thermodynamically favorable ($\Delta_rG(OH^- \rightarrow O_2) < 0$); (2) IO^- formation is never favorable versus the OER, while IO_3^- is always more thermodynamically favorable. This suggests that the kinetics associated with IO_3^- formation must also play a role in the observed switch from IO^-/IO_3^- formation to OER during charge. Given that the formation of IO_3^- is the thermodynamic product, and that it requires 3 equivalents of IO^- (Reaction 9), the rate at which this intermediate is formed is of paramount importance. Our results indicate that in water-containing glyme electrolytes, while the conversion to IO^- is still thermodynamically unfavorable, it occurs because there is no alternative competing OER reaction; its formation is likely driven by the driving force for IO_3^- formation. The introduction of $Pyr_{14}TFSI$ changes this equilibrium as the OER is now favorable. While IO_3^- remains the thermodynamic product, the kinetics of its formation involving the reaction of three IO^- molecules are unfavorable, which we suggest is key here. The kinetics of iodine redox reactions have been an intensely debated subject on its own for decades, with important ramifications to many fields,[44] which lies well outside of the scope of this article. It is, however, well understood that kinetically, iodine redox reactions are heavily dependent on the media. For instance, the iodine disproportionation reaction in aqueous media is greatly

reduced (by up to two orders of magnitude) at high pHs, at which the reaction becomes first order with respect to [IO^-].[44,45]

Our MD and ^{1}H-NMR results confirm that the introduction of the (soft Lewis base) Pyr_{14}^+ cation to the electrolyte has a strong impact on the coordination of the (soft Lewis acid) I^-, replacing H_2O, Li^+, and G4 to some extent in the environment of I^- (Figure 6E), in agreement with previous studies.[18,20] This suggests that the fast kinetics, of the IO^- formation in water-containing electrolytes, are disturbed by the introduction of Pyr_{14}TFSI due to efficient donor-acceptor interactions. Furthermore, as the MSD plot (Figure 6F) shows, there is a synergistic interaction between water and the Pyr_{14}^+ cation on the mobility of I^-, which could also play a kinetic role during the charge process.

Conclusions

LiI-mediated cells in the presence of water and the ionic liquid Pyr_{14}TFSI produce reversible 4 e^-/O_2 ORR and OER at 2.6 V and 3.2–3.5 V, respectively, during capacity-limiting galvanostatic cycling as monitored in *operando* OEMS experiments. A combination of *ex situ* characterization methods confirm that these reactions occur through the formation/decomposition of LiOH. OEMS experiments with Li_2O_2 preloaded electrodes show that the electrolyte mixture is also capable of efficiently decomposing Li_2O_2 through a 2 e^-/O_2 during OER. The presence of Pyr_{14}TFSI increases the I^-/I_3^- redox potential, shifting the mechanism of the LiOH OER from the irreversible production of IO^-/IO_3^- to the evolution of O_2. This shift in redox potential can be explained by a change in the solvation conditions of I^- in the presence of both water and the IL. Our NMR and MD results indicate that the combination of an IL and water in aprotic electrolytes is an effective strategy for tailoring the electrolyte properties and reaction mechanisms in redox-mediated Li-O_2 batteries. This study reopens the possibility of using LiOH as a viable, and water-resistant, discharge product in Li-air batteries. Further studies will be needed to understand all the intricate mechanistic details of this chemistry, as well as to improve the overall performance of the cell, especially with regard to rate and long-term reversibility.

EXPERIMENTAL PROCEDURES

Resource Availability

Lead Contact

Further information and requests for resources and reagents should be directed to and will be fulfilled by the Lead Contact, Clare P. Grey (cpg27@cam.ac.uk).

Materials Availability

This study did not generate new unique reagents.

Data and Code Availability

The solvation parameters used for implicit solvation DFT calculations are presented in the Supplemental Information.

Materials Preparation

Carbon electrodes were prepared by kneading a slurry made from 75 wt% carbon black (Ensaco P150, Imerys) and 25% PTFE binder (Aldrich, 60% water solution) in ethanol until a homogeneous film was obtained. Free-standing discs were cut from this film, annealed at 120°C *in vacuo* for 12 h, and transferred to the glovebox without exposure to air. The areal loading of the carbon electrode is ~1–2 mg/cm^2. Tetraethylene glycol dimethyl ether (G4, Aldrich, 99%) was refluxed with sodium metal under Ar for 3 days prior to fractional distillation *in vacuo*. The final water

content was measured by Karl Fischer titration (Metrohm) at <10 ppm and then stored over 4 Å molecular sieves. Lithium bis(trifluoromethyl)sulfonylimide (LiTFSI, 3M) and LiI (Aldrich, 99.9%) were dried *in vacuo* at 160°C and 200°C, respectively for 12 h before being used to prepare the electrolyte. 1-butyl-1-methyl-pyrrolidinium-bis-(trifluoromethanesulfonyl)-imide ($Pyr_{14}TFSI$, Solvionic 99.9%; $H_2O \leq 0.002\%$) was used as purchased. All materials were stored and handled in an Ar glovebox with <0.1 ppm O_2 and <0.1 ppm H_2O.

Electrochemical Methods

All Li-O_2 cells were assembled inside an Ar-filled glovebox on bored-through stainless steel Swagelok unions by staking a Li disc (PI-KEM, 99.99%), 1 piece of pressed borosilicate glass fiber separator (Whatman) wetted with 300 mM LiTFSI / G4 (anolyte), a disk of lithium-ion-conducting glass ceramic (LICGC; Ohara), 1 piece of pressed borosilicate glass fiber separator wetted with the active catholyte (90 μL in $^1/_2$" and 210 μL in 1" cells, respectively), and Ensaco P150 cathode. Stainless steel mesh (Advent) was used as a current collector. Electrochemical tests were performed on either a Biologic SP-300 or an Ivium Vertex potentiostat/galvanostat. Due to the significant overpotential induced by the use of a LICGC disk, the resistance of the cell was measured by impedance spectroscopy. Ohm's Law was then applied to obtain the Ohmic overpotential (Figure S20), which was then subtracted in the load curves. Galvanostatic cycling was limited to a current of 50 μA/cm^2 due to kinetic limitations of the very viscous electrolyte (Figures S9–S11, S18, and S19). A newly designed OEMS system was developed for this work, and it is described in detail in the Supplemental Information (Figure S1A). The cell design consists in a Swagelok-type cell with inlet and outlet tubes welded to the top plunger and capped with self-sealing quick-connects (Beswick Engineering) to isolate the cell from the atmosphere between assembly in the glovebox and connection to the OEMS system. Galvanostatic discharge and charge were carried out under 20% O_2 and 0% O_2 in Ar, respectively. A newly designed pressure-monitoring cell assembly was also developed for this work and is described in detail in the Supplemental Information (Figure S1B). A pressure transducer was connected to a Swagelok-type cell and sealed in the glovebox. The cell assembly was then pumped down and subsequently filled up with pure O_2. The total internal volume of the setup was measured independently for each test using a reference volume, and the measured change in pressure was then converted to number of moles of gas consumed using the ideal gas law.

Characterization Methods

Characterization of electrodes after electrochemical tests was performed by first disassembling the cell inside the glovebox, rinsing the cathode twice in G1, then drying them *in vacuo* at room temperature. Powder X-ray diffraction measurements were performed with the electrode placed in an air-tight sample holder in a Panalytical Empyrean diffractometer, in reflection mode with Cu Kα1 radiation (l = 1.5406 Å). Ultraviolet spectra were acquired on samples in an air-tight quartz cuvette in a PerkinElmer (LAMBDA TM 25/35) spectrometer. G4 was used for dilutions, and pristine electrolyte was used as reference. Scanning electron microscopy was obtained in a Tescan MIRA3 microscope (5 keV; 7 pA) with samples transported from the glovebox sealed in a Kammrath & Weiss transfer module. Solution ^{1}H-NMR spectra were acquired using an 11.7 T Bruker Avance III HD spectrometer with a single 30° (10.5 μs) flip angle pulse sequence - and with a recycle delay of 1 s. DMSO-d_6 was used as solvent. Titration experiments were performed following the method previously reported by McCloskey et al.[46] Cathodes were extracted from cells inside the glovebox and placed in a sealed vial unwashed. 2 mL of ultrapure water (Millipore) was

injected into the vial using a syringe, and then titration of the base was done with a standardized 10 mM HCl solution, using phenolphthalein as end-point indicator while vigorously stirring. The LiOH content is calculated based on this acid-base titration. Subsequently, 1 mL of KI (2 wt %), 1 mL of H_2SO_4 (3.5 M), and 50 mL of a molybdenum-based catalyst solution were added. The I_2 generated from the reaction of Li_2O_2, alongside the I_3^- present in the unwashed electrodes, was then quickly titrated using 0.01 N NaS_2O_3 solution using a starch indicator, in order to establish the presence or absence of Li_2O_2 in the discharge product (Figure S4). Post mortem measurement of water in electrolyte was measured in cells using Super P coated gas diffusion layer electrodes. The separator in the cathode side was wetted with 0.25 mL of electrolyte (containing 900 mM of IL and 5,000 ppm of water). The cells were then filled with O_2 (after 2 pumping/filling cycles) and investigated after resting, discharging, and charging to 2 mAh. Subsequently, the gas in the cells was evacuated by pumping for 30 min before introducing the cells into the glovebox for disassembly. The separator and electrode were then removed and stored in a vial in which 0.5 mL of G4 was used to wash the electrolyte. 0.3 mL of washed electrolyte was then collected and added to 34.4 mg LiTFSI to bring its concentration up to 700 mM (LiTFSI was added since its addition results in a shift of the water peak to higher ppm and into a range that does not overlap with the G4 peaks; see Figure S8), stirred for 2 mins, and left to rest for 24 h. ^{1}H-NMR of this solution was then collected, and the spectra was normalized with respect to the peak corresponding to the CH_2 groups of the IL.

Density Functional Theory Calculations

To obtain an understanding of the magnitude of the $\Delta_{sol}G()$ terms, DFT calculations were performed. In each case, the B3LYP-D3/def2-TZVP level of theory was used. The SMD solvation model[47] was used for implicit solvation calculations. The built-in parameters for water were used, while for G4 and $Pyr_{14}TFSI$, parameters were derived for the calculations (see Supplemental Information).

Molecular Dynamics Simulations

The simulation boxes were set up, using Packmol,[48] to be congruent with the experimental concentrations (700 mM LiTFSI, 50 mM LiI in G4, with 5,000 ppm of H_2O as starting point). Furthermore, water concentration was varied (0, 2,500, and 10,000 ppm of H_2O) as well as the presence/absence of the IL. The role of the concentration of the IL was also explored by varying the number of $Pyr_{14}TFSI$ molecules to be 0, 0.5, and 1.5 times the experimental concentration (0 mM, 450 mM, and 1,350 mM). The full list of values is presented in the Supplemental Information (Table S2). The time step in each simulation was 2 fs as the C-H bonds were fixed utilizing LINCS. The forcefield used was OPLS-AA, with additional parameters for $Pyr_{14}TFSI$ from CL&P.[49] The SPC water model was used. Scaled charges (to 0.8) were also used to speed up the simulation due to the inclusion of an IL in the system. The equilibration procedure was as follows: an initial starting run of 0.2 ns NVT (Nose-Hoover thermostat set to 298 K and 1 ps) followed by two NPT runs, both 4 ns long (the first one used the Berendsen barostat, set to 1 atm and 5 ps, and the second used the Parrinello-Rahman barostat). The two-step NPT procedure was used due a simulation instability when the Parrinello-Rahman barostat was used directly. The production runs were 10 ns NVT runs, storing output every 2,000 steps.

In each case, short-range cutoffs for non-bonded interactions were set to 1.2 nm. Gromacs versions 2018.2 and 2018.3 were used.[50] Analysis of the MD trajectories were done using the Gromacs toolchain, e.g., gmx rdf and gmx msd. The coordination number plots were done using the center of mass of each molecule.

SUPPLEMENTAL INFORMATION

Supplemental Information can be found online at https://doi.org/10.1016/j.joule.2020.09.021.

ACKNOWLEDGMENTS

This research was enabled by funding support from Innovate UK (132220) and the EPSRC (EP/M009521/1 DJR00640). The authors wish to acknowledge experimental contributions to this work by C. Brackstone for help with titration and UV spectroscopy, V. Kunz with water quantification, Dr. Y. Jin with ^{17}O-ssNMR characterization, and S. Engelke with cyclic voltammograms. T.L. acknowledges support from the Schlumberger Fellowship and Darwin College and Thousand Talent Recruitment Programme. E.J. acknowledges support from the Swedish Research Council in the form of an International Postdoc fellowship. Via our membership to the UK's HEC Materials Chemistry Consortium, which is funded by EPSRC (EP/L000202, EP/R029431), this work used the ARCHER UK National Supercomputing Service (http://www.archer.ac.uk).

AUTHOR CONTRIBUTIONS

I.T. contributed to project planning, data acquisition, analysis, and article writing; T.L. contributed to project planning; E.P. contributed to project planning and preliminary experiments; J.H.J.E. and G.K. contributed to data acquisition and analysis; E.J. contributed to theoretical data and analysis; C.P.G. contributed to project planning, supervision, and article writing. All authors contributed to the discussion of the results presented and editing.

DECLARATION OF INTERESTS

C.P.G. and T.L. have a patent pending associated with lithium-air technology.

Received: July 7, 2020
Revised: July 20, 2020
Accepted: September 30, 2020
Published: October 9, 2020

REFERENCES

1. Bose Styczynski, A., and Hughes, L. (2018). Public policy strategies for next-generation vehicle technologies: An overview of leading markets. Environ. Innov. Soc. Transit. *31*, 262–272.

2. Meckling, J., and Nahm, J. (2019). The politics of technology bans: Industrial policy competition and green goals for the auto industry. Energy Policy *126*, 470–479.

3. Grey, C.P., and Tarascon, J.M. (2016). Sustainability and in situ monitoring in battery development. Nat. Mater. *16*, 45–56.

4. Aurbach, D., McCloskey, B.D., Nazar, L.F., and Bruce, P.G. (2016). Advances in understanding mechanisms underpinning lithium–air batteries. Nat. Energy *1*, 16128.

5. Girishkumar, G., McCloskey, B., Luntz, A.C., Swanson, S., and Wilcke, W. (2010). Lithium—Air Battery: Promise and Challenges. J. Phys. Chem. Lett. *1*, 2193–2203.

6. Kwabi, D.G., Ortiz-Vitoriano, N., Freunberger, S.A., Chen, Y., Imanishi, N., Bruce, P.G., and Shao-Horn, Y. (2014). Materials challenges in rechargeable lithium-air batteries. MRS Bull. *39*, 443–452.

7. Liu, T., Vivek, J.P., Zhao, E.W., Lei, J., Garcia-Araez, N., and Grey, C.P. (2020). Current Challenges and Routes Forward for Nonaqueous Lithium-Air Batteries. Chem. Rev. *14*, 6558–6625.

8. Kwak, W.-J., Rosy, Sharon, D., Xia, C., Kim, H., Johnson, L.R., Bruce, P.G., Nazar, L.F., Sun, Y.-K., Frimer, A.A., et al. (2020). Lithium–Oxygen Batteries and Related Systems: Potential, Status, and Future. Chem. Rev. *14*, 6626–6683.

9. Mahne, N., Schafzahl, B., Leypold, C., Leypold, M., Grumm, S., Leitgeb, A., Strohmeier, G.A., Wilkening, M., Fontaine, O., Kramer, D., et al. (2017). Singlet oxygen generation as a major cause for parasitic reactions during cycling of aprotic lithium-oxygen batteries. Nat. Energy *2*, 17036.

10. Xia, C., Kwok, C.Y., and Nazar, L.F. (2018). A high-energy-density lithium-oxygen battery based on a reversible four-electron conversion to lithium oxide. Science *361*, 777–781.

11. Liu, T., Kim, G., Jónsson, E., Castillo-Martínez, E., Temprano, I., Shao, Y., Carretero-González, J., Kerber, R.N., and Grey, C.P. (2018). Understanding LiOH Formation in a Li-O_2 Battery with LiI and H_2O Additives. ACS Catal. *9*, 66–77.

12. Liu, T., Leskes, M., Yu, W., Moore, A.J., Zhou, L., Bayley, P.M., Kim, G., and Grey, C.P. (2015). Cycling Li-O_2 batteries via LiOH formation and decomposition. Science *350*, 530–533.

13. Liu, T., Liu, Z., Kim, G., Frith, J.T., Garcia-Araez, N., and Grey, C. (2017). Understanding LiOH Chemistry in a Ruthenium-Catalyzed Li–O_2 Battery. Angew. Chem. *129*, 16273–16278.

14. Burke, C.M., Black, R., Kochetkov, I.R., Giordani, V., Addison, D., Nazar, L.F., and McCloskey, B.D. (2016). Implications of 4 e– Oxygen Reduction via Iodide Redox Mediation in Li–O_2 Batteries. ACS Energy Lett. *1*, 747–756.

15. Qiao, Y., Wu, S., Sun, Y., Guo, S., Yi, J., He, P., and Zhou, H. (2017). Unraveling the Complex Role of Iodide Additives in Li–O_2 Batteries. ACS Energy Lett. *2*, 1869–1878.

16. Shen, Y., Zhang, W., Chou, S.-L., and Dou, S.-X. (2015). Comment on "Cycling Li-O_2 batteries via LiOH formation and decomposition". Science *352*, 667.

17. Viswanathan, V., Pande, V., Abraham, K.M., Luntz, A.C., McCloskey, B.D., and Addison, D. (2016). Comment on "Cycling Li-O_2 batteries via LiOH formation and decomposition". Science *352*, 667.

18. Bentley, C.L., Bond, A.M., Hollenkamp, A.F., Mahon, P.J., and Zhang, J. (2015). Voltammetric Determination of the Iodide/Iodine Formal Potential and Triiodide Stability Constant in Conventional and Ionic Liquid Media. J. Phys. Chem. C *119*, 22392–22403.

19. Leverick, G., Tulodziecki, M., Tatara, R., Bardé, F., and Shao-Horn, Y. (2019). Solvent-Dependent Oxidizing Power of LiI Redox Couples for Li-O_2 Batteries. Joule *3*, 1106–1126.

20. Nakanishi, A., Thomas, M.L., Kwon, H.-M., Kobayashi, Y., Tatara, R., Ueno, K., et al. (2018). Electrolyte Composition in Li/O_2 Batteries with LiI Redox Mediators: Solvation Effects on Redox Potentials and Implications for Redox Shuttling. J. Phys. Chem. C *122*, 1522–1534.

21. Wu, S., Tang, J., Li, F., Liu, X., Yamauchi, Y., Ishida, M., and Zhou, H. (2016). A Synergistic System for Lithium–Oxygen Batteries in Humid Atmosphere Integrating a Composite Cathode and a Hydrophobic Ionic Liquid-Based Electrolyte. Adv. Funct. Mater. *26*, 3291–3298.

22. Allen, C.J., Hwang, J., Kautz, R., Mukerjee, S., Plichta, E.J., Hendrickson, M.A., and Abraham, K.M. (2012). Oxygen Reduction Reactions in Ionic Liquids and the Formulation of a General ORR Mechanism for Li–Air Batteries. J. Phys. Chem. C *116*, 20755–20764.

23. Elia, G.A., Hassoun, J., Kwak, W.J., Sun, Y.K., Scrosati, B., Mueller, F., Bresser, D., Passerini, S., Oberhumer, P., Tsiouvaras, N., and Reiter, J. (2014). An advanced lithium-air battery exploiting an ionic liquid-based electrolyte. Nano Lett. *14*, 6572–6577.

24. Piana, M., Wandt, J., Meini, S., Buchberger, I., Tsiouvaras, N., and Gasteiger, H.A. (2014). Stability of a Pyrrolidinium-Based Ionic Liquid in Li-O_2 Cells. J. Electrochem. Soc. *161*, A1992–A2001.

25. Shimizu, K., Freitas, A.A., Atkin, R., Warr, G.G., FitzGerald, P.A., Doi, H., Saito, S., Ueno, K., Umebayashi, Y., Watanabe, M., and Canongia Lopes, J.N. (2015). Structural and aggregate analyses of (Li salt + glyme) mixtures: the complex nature of solvate ionic liquids. Phys. Chem. Chem. Phys. *17*, 22321–22335.

26. Elia, G.A., Bernhard, R., and Hassoun, J. (2015). A lithium-ion oxygen battery using a polyethylene glyme electrolyte mixed with an ionic liquid. RSC Adv. *5*, 21360–21365.

27. Amanchukwu, C.V., Chang, H.-H., Gauthier, M., Feng, S., Batcho, T.P., and Hammond, P.T. (2016). One-Electron Mechanism in a Gel–Polymer Electrolyte Li–O_2 Battery. Chem. Mater. *28*, 7167–7177.

28. Mozhzhukhina, N., Tesio, A.Y., De Leo, L.P.M., and Calvo, E.J. (2017). In Situ Infrared Spectroscopy Study of $PYR_{14}TFSI$ Ionic Liquid Stability for Li–O_2 Battery. J. Electrochem. Soc. *164*, A518–A523.

29. Monaco, S., Soavi, F., and Mastragostino, M. (2013). Role of Oxygen Mass Transport in Rechargeable Li/O_2 Batteries Operating with Ionic Liquids. J. Phys. Chem. Lett. *4*, 1379–1382.

30. Liu, T., Frith, J.T., Kim, G., Kerber, R.N., Dubouis, N., Shao, Y., Liu, Z., Magusin, P.C.M.M., Casford, M.T.L., Garcia-Araez, N., and Grey, C.P. (2018). The Effect of Water on Quinone Redox Mediators in Nonaqueous Li-O_2 Batteries. J. Am. Chem. Soc. *140*, 1428–1437.

31. Meini, S., Solchenbach, S., Piana, M., and Gasteiger, H.A. (2014). The Role of Electrolyte Solvent Stability and Electrolyte Impurities in the Electrooxidation of Li_2O_2 in Li-O_2 Batteries. J. Electrochem. Soc. *161*, A1306–A1314.

32. Mu, X., Jiang, J., Deng, H., Qiao, Y., Zheng, M., Zhang, X., et al. (2019). H_2O self-trapping air cathode of Li–O_2 battery enabling low charge potential operating in dry system. Nano Energy *64*, 103945.

33. Qiao, Y., Wu, S., Yi, J., Sun, Y., Guo, S., Yang, S., et al. (2017). From O_2^- to HO_2^-: Reducing By-Products and Overpotential in Li-O_2 Batteries by Water Addition. Angew. Chem. Int. Ed. *56*, 4960–4964.

34. Tulodziecki, M., Leverick, G.M., Amanchukwu, C.V., Katayama, Y., Kwabi, D.G., Barde, F., Hammond, P.T., and Shao-Horn, Y. (2017). The role of iodide in the formation of lithium hydroxide in lithium–oxygen batteries. Energy Environ. Sci. *10*, 1828–1842.

35. Haskins, J.B., Yildirim, H., Bauschlicher, C.W., and Lawson, J.W. (2017). Decomposition of Ionic Liquids at Lithium Interfaces. 2. Gas Phase Computations. J. Phys. Chem. C *121*, 28235–28248.

36. Yildirim, H., Haskins, J.B., Bauschlicher, C.W., and Lawson, J.W. (2017). Decomposition of Ionic Liquids at Lithium Interfaces. 1. *Ab Initio* Molecular Dynamics Simulations. J. Phys. Chem. C *121*, 28214–28234.

37. Mohzhukhina, N., Tesio, A.Y., Pozo, M.d., and Calvo, E.J. (2017). Communication—Lithium Ion Concentration Effect in $PYR_{14}TFSI$ Ionic Liquid for Li-O_2 Battery Cathodes. J. Electrochem. Soc. *164*, H5277–H5279.

38. Gallant, B.M., Kwabi, D.G., Mitchell, R.R., Zhou, J., Thompson, C.V., and Shao-Horn, Y. (2013). Influence of Li_2O_2 morphology on oxygen reduction and evolution kinetics in Li–O_2 batteries. Energy Environ. Sci. *6*, 2518–2528.

39. Lu, Y.-C., and Shao-Horn, Y. (2013). Probing the Reaction Kinetics of the Charge Reactions of Nonaqueous Li-O2 Batteries. J. Phys. Chem. Lett. *4*, 93–99.

40. McCloskey, B.D., Bethune, D.S., Shelby, R.M., Girishkumar, G., and Luntz, A.C. (2011). Solvents' Critical Role in Nonaqueous Lithium-Oxygen Battery Electrochemistry. J. Phys. Chem. Lett. *2*, 1161–1166.

41. J. Rumble, ed. (2019). CRC Handbook of Chemistry and Physics (CRC Press).

42. Pearson, R.G. (1963). Hard and Soft Acids and Bases. J. Am. Chem. Soc. *85*, 3533–3539.

43. Liu, T., Kim, G., Carretero-González, J., Castillo-Martínez, E., and Grey, C.P. (2016). Response to Comment on "Cycling Li-O_2 batteries via LiOH formation and decomposition". Science *352*, 667.

44. Truesdale, V.W., Luther, G.W., and Greenwood, J.E. (2003). The kinetics of iodine disproportionation: a system of parallel second-order reactions sustained by a multi-species pre-equilibrium. Phys. Chem. Chem. Phys. *5*, 3428–3435.

45. Truesdale, V.W., Canosa-Mas, C., and Luther Iii, G.W. (1994). Kinetics of disproportionation of hypoiodous acid. J. Chem. Soc., Faraday Trans. *90*, 3639–3643.

46. McCloskey, B.D., Valery, A., Luntz, A.C., Gowda, S.R., Wallraff, G.M., Garcia, J.M., et al. (2013). Combining Accurate O_2 and Li_2O_2 Assays to Separate Discharge and Charge Stability Limitations in Nonaqueous Li-O_2 Batteries. J. Phys. Chem. Lett. *4*, 2989–2993.

47. Marenich, A.V., Cramer, C.J., and Truhlar, D.G. (2009). Universal solvation model based on solute electron density and on a continuum model of the solvent defined by the bulk dielectric constant and atomic surface tensions. J. Phys. Chem. B *113*, 6378–6396.

48. Martínez, L., Andrade, R., Birgin, E.G., and Martínez, J.M. (2009). PACKMOL: a package for building initial configurations for molecular dynamics simulations. J. Comput. Chem. *30*, 2157–2164.

49. Canongia Lopes, J.N., and Padua, A.A.H. (2004). Molecular Force Field for Ionic Liquids Composed of Triflate or Bistriflylimide Anions. J. Phys. Chem. B *108*, 16893–16898.

50. Abraham, M.J., Murtola, T., Schulz, R., Szilard, P., Smith, J.C., Hess, B., and Lindahl, E. (2015). GROMACS: High performance molecular simulations through multi-level parallelism from laptops to supercomputers. SoftwareX *1-2*, 19–25.